Numerical comparison of BGK-models with proper Prandtl number

Luc Mieussens

UFR MIG, Universite Paul Sabatier Toulouse 3
118 route de Narbonne, 31062 Toulouse cedex 4, France

Henning Struchtrup

Department of Mechanical Engineering, University of Victoria
PO Box STN CSC 3055, Victoria BC V8W 3P6, Canada, e-mail: struchtr@me.uvic.ca

Abstract

While the standard BGK model leads to the wrong Prandtl number, the BGK-model with velocity dependent collision frequency as well as the Ellipsoidal Statistical BGK model can be adjusted to give its proper value of 2/3. In this paper, the BGK model with velocity dependent collision frequency is considered in some detail. The corresponding thermal conductivity and viscosity are computed from the Chapman-Enskog method, and several velocity-dependent collision frequencies are introduced which all give the proper Prandtl number. The models are tested for Couette flow, and the results are compared to solutions obtained with the ES-BGK model, and the Direct Simulation Monte Carlo method. The simulations rely on a numerical scheme that ensures positivity of solutions, conservation of moments, and dissipation of entropy. The advantages and disadvantages of the various BGK models are discussed.

I. INTRODUCTION

Because of its simplicity compared to the Boltzmann equation the BGK equation is widely used in the kinetic theory of gases[1,2]. While the BGK equation gives qualitatively good results, it fails when one is interested in quantitatively correct results. This fact manifests itself most prominently in the computation of the Prandtl number, i.e. the dimensionless ratio of viscosity and thermal conductivity. While measurements and the theory of the full Boltzmann equation give $\mathrm{Pr} \simeq \frac{2}{3}$, one obtains $\mathrm{Pr} = 1$ from the standard BGK model[3].

There are two main approaches to modify the BGK model in order to obtain the proper Prandtl number: the Gaussian BGK-model, or ellipsoidal statistical model (ES-BGK model)[4,5], and the BGK-model with velocity dependent collision frequency[6,7].

In all three approaches, standard BGK, ES-BGK, and BGK with velocity-dependent collision frequency, the Boltzmann collision term is replaced by a relaxation type term of the form

$$\mathcal{S}_{BGK} = -\nu\,(f - f_E)$$

where ν is the collision frequency, f is the actual distribution function of the microscopic velocities of the gas, and f_E is a suitable equilibrium phase density. In standard and ES-BGK models the collision frequency is independent of the microscopic velocity, and its value is obtained from fitting to viscosity data. These two approaches differ in the equilibrium function f_E: in the standard BGK model f_E is the local Maxwell distribution f_M, i.e. an isotropic Gaussian, while in the ES-BGK model f_E is a local anisotropic Gaussian. In the BGK model with velocity-dependent collision frequency, ν is a function of the microscopic velocity C of the particles and f_E is a local isotropic Gaussian, albeit not the local Maxwellian.

The BGK model with velocity-dependent collision frequency is briefly discussed in the book of Cercignani[3], and Bouchut and Perthame discussed it thoroughly from a mathematical viewpoint[6]. In both references, however, the form of the collision frequency was not discussed. To our best knowledge, the first attempt to consider an explicit expression for $\nu\,(C)$ can be found in a paper by Struchtrup[7] who considered the simplest possible ansatz,

namely $\nu(C) \sim C^n$. The proper Prandtl number is obtained for $n \simeq 1.79$. In the present paper, we present some alternative functions for the collision frequency, which lead to the proper Prandtl number, but, however, do not agree with realistic collision frequency of particles. We also show that the combination of BGK model with realistic collision frequencies cannot give the proper value of Pr.

The BGK equations for the different models are solved for Couette flow at various Knudsen numbers. The results will be compared with solutions obtained from the standard and the ES-BGK models, and with Direct Simulation Monte Carlo computations (DSMC).

The numerical method used for solving the various BGK equations considered here is the method of Mieussens[8–10]. The great advantage of this method compared to others is that it guarantees the conservation of mass, momentum, and energy.

The main goal of this paper is to study whether BGK models can be used to model flows over a wider range of Knudsen numbers. The BGK models with proper Prandtl number are constructed such that they give accurate results for small Knudsen numbers, that is in the hydrodynamic regime, where the laws of Navier-Stokes and Fourier are applicable. It is not clear a priori, whether the BGK models can give accurate results in the transition regime, where the Navier-Stokes-Fourier theory fails. The results presented below indicate that BGK models can give qualitatively good results, but have some problems to quantitatively describe flows at larger Knudsen numbers, where the details of the collision frequency become important. Of course, models with proper Prandtl number can cover a wider range of Knudsen numbers than the standard BGK model, and must be preferred over the latter.

However, only further improvement of the models, that would allow the use of the real collision frequencies, can render the BGK models into a tool that gives accurate results over a wide range of Knudsen numbers. Here it must be mentioned that the use of BGK models allows to obtain deterministic results, rather than statistical results that suffer from noise as in the DSMC method. Also, numerical solutions of BGK models can be obtained faster than solutions for the full Boltzmann equation, which is nonlinear. Note also that the numerical scheme of this paper guarantees conservation of mass, momentum and energy irrespective

of the numerical accuracy.

The remainder of the paper is organized as follows: In Section 2 we introduce various BGK models. In particular, we show that the BGK models with velocity dependent collision frequency have the same characteristics as the full Boltzmann collision term, we discuss how to obtain viscosity and heat conductivity by means of the Chapman-Enskog method, and we introduce several models for the collision frequency. In Section 3 we discuss details of the numerical method, and in Section 4 we give and discuss numerical results for Couette flow at Knudsen numbers between 0.012 and 1.2. The paper ends with our conclusions.

II. BGK MODELS

A Phase density and Boltzmann equation

The state of a monatomic ideal gas is completely described when the phase density $f(x_i, t, c_i)$ is known[3] which is defined such that $f d\mathbf{c}$ gives the number density of atoms with velocity in $(c_i, c_i + dc_i)$ at place x_i and time t.

The macroscopic quantities density ϱ, velocity v_i, density of internal energy $\varrho\varepsilon$, pressure tensor $p_{\langle ij\rangle}$, and heat flux vector q_i of the gas are given by moments of the phase density,

$$\varrho = m\int f d\mathbf{c}\ ,\quad \varrho v_i = m\int c_i f d\mathbf{c}\ ,\quad \varrho\varepsilon = \frac{3}{2}\varrho\frac{k}{m}T = \frac{m}{2}\int C^2 f d\mathbf{c}$$
$$p_{\langle ij\rangle} = m\int C_{\langle i}C_{j\rangle} f d\mathbf{c}\ ,\quad q_i = \frac{m}{2}\int C^2 C_i f d\mathbf{c} \tag{1}$$

where m is the mass of one particle, k is Boltzmann's constant, and $C_i = c_i - v_i$ is the peculiar velocity. T is the gas temperature, which is defined by Eqn. $(1)_3$. The entropy of the gas is given by

$$\varrho s = -k\int f \ln f d\mathbf{c}.$$

The phase density $f(x_i, t, c_i)$ is governed by the Boltzmann equation[3,11],

$$\frac{\partial f}{\partial t} + c_i\frac{\partial f}{\partial x_i} = \mathcal{S}\ . \tag{2}$$

where $\mathcal{S}$ is the collision term which has the following four properties[3]

i.) It guarantees the conservation of mass, momentum and energy, which may be written as

$$\int m\mathcal{S}d\mathbf{c} = 0 \ , \quad \int mc_i\mathcal{S}d\mathbf{c} = 0 \ , \int \frac{m}{2}c^2\mathcal{S}d\mathbf{c} = 0 \ . \tag{3}$$

ii.) The production of entropy is always positive (H-Theorem),

$$-k\int \ln f\mathcal{S}d\mathbf{c} \geqslant 0 \ .$$

iii.) Due to the specific form of $\mathcal{S}$ the phase density in equilibrium is a Maxwellian, i.e.

$$\mathcal{S} = 0 \Longrightarrow f = f_M = \frac{\varrho}{m}\sqrt{\frac{m}{2\pi kT}}^3 \exp -\frac{m}{2kT}C^2 \ .$$

iv.) The Prandtl number is close to $\frac{2}{3}$ for all physically meaningful collision factors σ, i.e.

$$\mathrm{Pr} = \frac{5}{2}\frac{k}{m}\frac{\mu}{\kappa} \simeq \frac{2}{3}$$

where μ and κ denote viscosity and thermal conductivity, respectively.

B The BGK equation

Because of its complex non-linearity, the Boltzmann collision term $\mathcal{S}$ is difficult to handle. Therefore one is interested in model equations which are easier to handle than the Boltzmann equation but which should also have the properties i.) through iv.). The most used model is the BGK equation, see Refs. 12,7 for a motivation. The BGK collision term reads

$$\mathcal{S}_\gamma = -\nu\left(f - f_\gamma\right) \tag{4}$$

where f_γ is a Gaussian

$$f_\gamma = a\exp\left(-\Gamma C^2 + \gamma_i C_i\right) \ , \tag{5}$$

and ν denotes the collision frequency which is given by

$$\nu\left(x_i, t, C\right) = \int f_\gamma^1 \sigma g \sin\theta d\theta d\theta d\varepsilon d\mathbf{c}_1 \ . \tag{6}$$

Here, $g = |\mathbf{c} - \mathbf{c}^1|$ is the relative velocity of colliding particles, σ is the scattering factor, ε and θ are the angles of collision. The collision frequency is a function of the microscopic velocity C (through σ and g) which is evaluated for the case of hard spheres and equilibrium in Ref. 13, we shall discuss it in Section 2.5 below.

The coefficients a, Γ, γ_i for the distribution (5) follow from the conservation conditions (3), where $\mathcal{S}$ must be replaced by $\mathcal{S}_\gamma$. Note, that f_γ is only a Maxwellian if ν does not depend on the peculiar velocity C_i.

It should be emphasized that — because of the conditions (3) — the BGK equation, i.e. the Boltzmann equation with the collision term (4), is a non-linear integro-differential equation, just like the Boltzmann equation. So one will not expect analytical solutions. But as we will show, the standard procedures of the Chapman-Enskog expansion are much easier to perform for the BGK equation than for the Boltzmann equation. It is straight forward to show that the BGK equation shares the properties i.), ii.), iii.) with the Boltzmann equation[3,7]. The calculation of the Prandtl number (property iv.) will be performed in the next sections of the paper. But one may conjecture easily that the extension of the ordinary BGK model to the case where ν is a function of C offers an additional degree of freedom which may be used to adjust both, viscosity and thermal conductivity, to their measured values.

C ES-BGK model

In order to obtain the proper Prandtl number, Holway suggested the so-called ellipsoidal statistical BGK model (ES-BGK model), where the Maxwellian of the standard BGK model is replaced by an anisotropic Gaussian[4] so that the collision term reads

$$\mathcal{S} = -\nu\,(f - f_G)$$

where f_G denotes the anisotropic Gaussian

$$f_G = \frac{\rho}{m}\frac{1}{\sqrt{\det\left[2\pi\lambda_{ij}\right]}}\exp\left[-\frac{1}{2}\lambda_{ij}^{-1}C_iC_j\right]\ ,$$

and the matrix λ_{ij} is given by

$$\lambda_{ij} = RT\delta_{ij} + \left(1 - \frac{1}{\mathrm{Pr}}\right)\frac{p_{\langle ij\rangle}}{\rho} \; ;$$

λ_{ij}^{-1} denotes the inverse matrix. While it is relatively straightforward to show that this model fulfills the conditions i.),iii.) and iv.) of Section 2.1, the proof of condition ii.) (H-Theorem), is non-trivial, and was only recently presented by Andries et al.[5]. The ES-BGK model assumes that the collision frequency is independent of the microscopic velocity.

D Chapman-Enskog method

The BGK equation follows from (2) after replacement of $\mathcal{S}$ by $\mathcal{S}_\gamma$ as

$$\frac{\partial f}{\partial t} + c_i\frac{\partial f}{\partial x_i} = -\nu\left(f - f_\gamma\right) \; . \tag{7}$$

We proceed by calculating the phase density f from Eqn. (7) by means of the Chapman-Enskog method[3]. The first order Chapman-Enskog expansion relies on the assumption that the phase density is close to a Maxwellian, i.e. $f \simeq f_M\left(1+\phi\right)$, where $\phi \ll 1$. In this case, the equilibrium distribution f_γ will be close to equilibrium as well, so that $f_\gamma = f_M\left(1+\phi_\gamma\right)$ with $\phi_\gamma \ll 1$. In fact, we can write

$$f_\gamma = \frac{\varrho}{m}\sqrt{\frac{m}{2\pi kT}}^3\left(1-\hat{a}\right)\exp\left[-\left(\frac{m}{2kT} - \hat{\Gamma}\right)C^2 + \gamma_i C_i\right] \simeq f_M\left[1 - \hat{a} + \hat{\Gamma}C^2 + \gamma_i C_i\right] \; .$$

where the coefficients $\hat{a}$, γ_i, $\hat{\Gamma}$ measure the deviation from the Maxwellian and are assumed to be small.

We insert the Maxwell phase density on the left hand side of (7) and eliminate all time derivatives by means of the Euler equations for monatomic gases,

$$\dot{\varrho} + \varrho\frac{\partial v_k}{\partial x_k} = 0 \;\; , \quad \dot{v}_i + \frac{1}{\varrho}\frac{\partial \varrho\frac{k}{m}T}{\partial x_i} = 0 \;\; , \quad \left(\frac{T^{\frac{3}{2}}}{\varrho}\right)^{\bullet} = 0 \; .$$

After some rearrangement of the resulting equation we find for the phase density

$$f = f_\gamma - \frac{1}{\nu}f_M\left\{\frac{m}{kT}\frac{\partial v_{\langle i}}{\partial x_{j\rangle}}C_{\langle i}C_{j\rangle} + \frac{1}{T}\frac{\partial T}{\partial x_i}\left(\frac{m}{2kT}C^2 - \frac{5}{2}\right)C_i\right\} \; . \tag{8}$$

It is remarkable that this approximate solution fulfills the conservation conditions (3) for *any* distribution f_γ. Thus, the coefficients $\hat{a}$, γ_i, $\hat{\Gamma}$ cannot be determined from these conditions. However, the phase density (8) must reproduce the first moments $(1)_{1-3}$ and it follows that $\hat{a} = \hat{\Gamma} = 0$ and

$$\gamma_i = \frac{8}{3\sqrt{\pi}} \frac{1}{T} \frac{\partial T}{\partial x_i} \int \frac{\eta^4 \left(\eta^2 - \frac{5}{2}\right)}{\nu\left(\eta\right)} e^{-\eta^2} d\eta \ ,$$

where $\eta = \sqrt{\frac{m}{2kT}} C$. Pressure deviator $p_{\langle ij \rangle}$ and heat flux vector q_i follow from evaluating their definitions (1) with the Chapman-Enskog phase density (8). This yields the laws of Navier-Stokes and Fourier with explicit expressions for viscosity μ and thermal conductivity κ,

$$\begin{aligned} p_{\langle ij \rangle} &= -\underbrace{\frac{32}{15\sqrt{\pi}} \varrho \frac{k}{m} T \int \frac{\eta^6}{\nu\left(\eta\right)} e^{-\eta^2} d\eta}_{2\mu} \frac{\partial v_{\langle i}}{\partial x_{j\rangle}} \ , \\ q_i &= -\underbrace{\frac{8}{3\sqrt{\pi}} \varrho \frac{k^2}{m^2} T \int \frac{\eta^4 \left(\eta^2 - \frac{5}{2}\right)^2}{\nu\left(\eta\right)} e^{-\eta^2} d\eta}_{\kappa} \frac{\partial T}{\partial x_i} \ . \end{aligned} \tag{9}$$

As expected, the Prandtl number depends on the collision frequency

$$\mathrm{Pr} = \frac{5}{2} \frac{k}{m} \frac{\mu}{\kappa} = \frac{\int \frac{\eta^6}{\nu(\eta)} e^{-\eta^2} d\boldsymbol{\eta}}{\int \frac{\eta^4 \left(\eta^2 - \frac{5}{2}\right)^2}{\nu(\eta)} e^{-\eta^2} d\eta} \ . \tag{10}$$

E Collision frequencies

Now we discuss the collision frequency as function of the microscopic velocity. Due to the severe simplifications in the derivation of the BGK equation, we cannot expect that the collision frequency (6) will give us the proper Prandtl number. While we shall adopt ad hoc models for the collision frequency later, it is instructive to study the original collision frequency (6) first. We consider close to equilibrium situations, where we can replace f_γ^1 by the Maxwellian f_M so that

$$\nu\left(C\right) = \int f_M^1 \sigma g \sin\theta d\theta d\varepsilon d\mathbf{c}_1 \ .$$

For power interaction potentials between particles $\phi \sim r^{-(n-1)}$, one can show[11] that

$$\sigma g \sin\theta d\theta = g^{\frac{n-5}{n-1}} s_0 ds_0$$

where $s_0 = s_0(\theta)$ and n gives the order of the potential. $n = 5$ represents the so-called Maxwell molecules while $n \to \infty$ describes hard spheres.

The above integral can be reduced to

$$\nu_n(\eta) = 2\pi\nu_0 \frac{n-1}{3n-7} \int_{\xi=0}^{\infty} \frac{\xi e^{-\xi^2}}{\eta} \left[(\xi+\eta)^{\frac{3n-7}{n-1}} - |\xi-\eta|^{\frac{3n-7}{n-1}} \right] d\xi. \tag{11}$$

$$\text{where} \quad \nu_0 = \frac{\varrho}{m\pi^{3/2}} \sqrt{\frac{2kT}{m}}^{\frac{n-5}{n-1}} \int s_0 ds_0 d\varepsilon \ ;$$

$\xi_i = C_i^1 / \sqrt{\frac{2kT}{m}}$, $\eta_i = C_i / \sqrt{\frac{2kT}{m}}$ are dimensionless velocities. For Maxwell molecules ($n = 5$) the collision frequency is independent of the particle velocity,

$$\nu_{Maxwell} = 4\pi\nu_0 \int_{\xi=0}^{\infty} e^{-\xi^2} \xi^2 d\xi = \pi^{3/2}\nu_0 \ ,$$

and for hard spheres ($n = \infty$) one finds[13]

$$\nu_{HS}(C) = \pi\nu_0 \left\{ e^{-\eta^2} + \frac{\sqrt{\pi}}{2} \left(\frac{1}{\eta} + 2\eta \right) \operatorname{erf}\eta \right\} \ .$$

For other values of n, the collision frequency must be integrated numerically, and Fig. 1 shows the normalized dimensionless collision frequency as function of the dimensionless velocity $\eta = C / \sqrt{\frac{2kT}{m}}$ for a variety of values of n. It can be seen that ν is a monotonous increasing function of speed. This indeed meets the expectations: fast particles should collide more often and should therefore have a larger collision frequency. The constant collision frequency of Maxwell molecules corresponds to the standard BGK model with constant ν.

The Prandtl number (10) for various power potentials can be obtained from further analytical or numerical integration. For Maxwell molecules (constant ν) we find the usual result of the BGK model $\mathrm{Pr}_{Maxwell} = 1$. For increasing values of n, the Prandtl number increases slightly to a maximum of 1.01615 at $n \simeq 13$ and is then decreasing to 1.0126 for hard spheres. Since the proper Prandtl number is 2/3, it follows that the collision frequencies

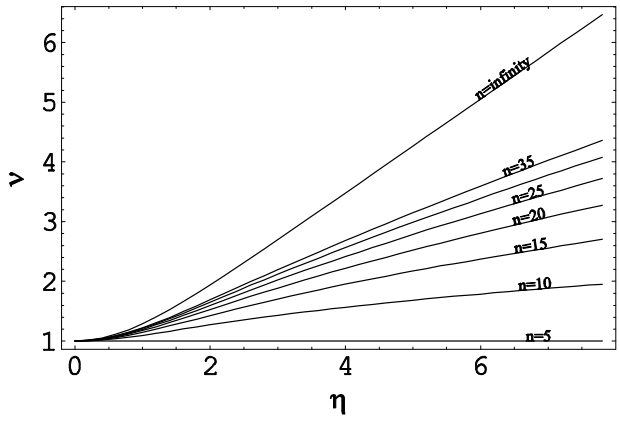

FIG. 1: The dimensionless and normalized collision frequency ν as a function of dimensionless microscopic velocity η for a variety of power potentials with exponent n.

for power potentials give the wrong Prandtl number and therefore do not improve the BGK model.

There is an infinite number of possible functions $\nu(\eta)$ which give the proper Prandtl number. Since the true collision frequency is an increasing function in η, we consider only increasing functions. We introduce the following notation

$$\nu(\eta) = \frac{\varrho \frac{k}{m} T}{\mu} \hat{\nu}(\eta) \quad \text{with} \quad \frac{16}{15\sqrt{\pi}} \int \frac{\eta^6}{\hat{\nu}(\eta)} e^{-\eta^2} d\boldsymbol{\eta} = 1 \,, \tag{12}$$

see the definition of viscosity (9). In 7 we presented the simple power law

$$\hat{\nu}_1(\eta) = 0.431587\, \eta^{1.791288}$$

which yields $\mathrm{Pr} = 2/3$. While $\nu_1(\eta)$ is the flattest polynomial we could find, it is unphysical as it states that a particle at rest ($\eta = 0$) would not undergo collisions and stay at rest forever. However, these particles will collide with particles of non-zero velocity, and therefore $\nu(\eta = 0)$ should be non-zero. Three simple functions which fulfill this requirement and give

Pr = 2/3 are

$$\hat{\nu}_2(\eta) = 0.0268351\left(1 + 14.2724\eta^2\right) ,$$
$$\hat{\nu}_3(\eta) = 0.0365643\left(1 + 10\eta^{2.081754}\right) ,$$
$$\hat{\nu}_4(\eta) = 0.1503991\left(1 + 0.92897\eta^4\right) .$$

A simple discontinuous function which gives the proper Prandtl number is

$$\hat{\nu}_5(\eta) = \begin{cases} 0.2590894 & , \ \eta \leq 1.2 \\ \\ 0.8288236\,\eta & \eta > 1.2 \end{cases}$$

For hard sphere molecules, we find $\hat{\nu}_{HS}(0) = 0.557608$ for molecules at rest and $\hat{\nu}_{HS}(\eta \gg 1) = 0.4941673\,\eta$ for fast particles. Thus, in comparison to hard sphere molecules, all of our models underestimate the collision frequency for slower particles ($\eta \lesssim 1.5$) and overestimate that of faster particles ($\eta \gtrsim 1.5$).

F Viscosity, mean free path, and Knudsen number

As can be seen from Eqn. (12), data for the viscosity μ is required to completely define the collision frequency ν. For ideal gases the viscosity is a function of temperature alone, and for our calculation we assume that

$$\mu(T) = \mu_0 \left(\frac{T}{T_0}\right)^{\omega} \tag{13}$$

where μ_0 is the viscosity at the reference temperature T_0 and ω is a positive number of order unity. For details, see the book by Bird[14], where values for μ_0 and ω are tabulated.

The mean free path of a particle with velocity c is given by

$$\lambda(c) = \frac{c}{\nu(c)}$$

and accordingly the mean free path of all particles is

$$\bar{\lambda} = \frac{\int \lambda(c)\, f d\mathbf{c}}{\int f d\mathbf{c}} .$$

Evaluating in equilibrium where f is a Maxwellian, we find

$$\bar{\lambda} = \frac{\mu}{p}\sqrt{\frac{2kT}{m}}\frac{4}{\sqrt{\pi}}\int \frac{\eta^3}{\hat{\nu}\left(\eta\right)}e^{-\eta^2}d\eta \; . \tag{14}$$

The Knudsen number Kn is defined as the ratio between the mean free path $\bar{\lambda}$ of a particle, and a characteristic macroscopic length L of the problem under consideration, that is $\mathrm{Kn} = \bar{\lambda}/L$. With the mean free path as above, the Knudsen number depends on microscopic details of the particle interaction, in particular the collision frequency. However, it is customary in kinetic theory to define a Knudsen number that depends only on macroscopic parameters by[3]

$$\mathrm{Kn} = \frac{\mu}{pL}\sqrt{\frac{\pi}{2}\frac{kT}{m}} \; . \tag{15}$$

This definition allows to compare results obtained with different microscopic models (in our case different functions $\hat{\nu}\left(\eta\right)$), but with the same macroscopic properties, p, T, μ.

From the definition of the mean free path (14) follows the Knudsen number $\overline{\mathrm{Kn}}$ as

$$\overline{\mathrm{Kn}} = \frac{\bar{\lambda}}{L} = \chi\,\mathrm{Kn} \qquad \text{where} \qquad \chi = \frac{8}{\pi}\int \frac{\eta^3}{\hat{\nu}\left(\eta\right)}e^{-\eta^2}d\eta \; . \tag{16}$$

The values of the number χ for the different models are given below

	ν_{DSMC}	ν_{BGK}	ν_{ES-BGK}	ν_1	ν_2	ν_3	ν_4	ν_5
χ_α	0.77177	1.27324	1.90986	2.80147	2.78725	2.79262	3.00385	2.64

The value for χ_{DSMC} was obtained from Ref. 14 - the Knudsen number given there corresponds to our $\overline{\mathrm{Kn}}$. The value for the ES-BGK model follows since in the ES-BGK model viscosity and constant collision frequency are related as $\nu = \frac{2}{3}\frac{p}{\mu}$.

It follows that gases with the same macroscopic properties, and therefore the same Knudsen number Kn, have different values of the mean free path based Knudsen number $\overline{\mathrm{Kn}}$. From the table we see that that the Knudsen numbers $\overline{\mathrm{Kn}}$ for the ad-hoc models ν_1 to ν_5 are more than twice the Knudsen number $\overline{\mathrm{Kn}}$ for DSMC calculations.

III. NUMERICAL METHOD

Many works have been devoted to numerical solutions of BGK models (e.g. see Ref. 15 and the references therein). However, in our new BGK models, the collision frequency can reach very large values and this can lead to numerical difficulties (lack of robustness, slow convergence). We believe that an alternate method proposed by one of the authors in Ref. 10 is better adapted to such problems. We briefly recall the main ideas of this method in this section.

A Explicit scheme

For the sake of simplicity, our numerical method is presented in one spatial dimension, but three dimensions in microscopic velocity; see Refs. 9 and 10 for a complete description.

The equation to be approximated is

$$\frac{\partial f}{\partial t} + c_x \frac{\partial f}{\partial x} = -\nu(f - f_\gamma), \qquad 0 \leq x \leq L. \tag{17}$$

The space variable x is discretized on a uniform grid defined by nodes $x_i = i\Delta x$ with $x_0 = 0$ and $x_I = L$. The velocity c_x is discretized by nodes $c_x^{(j_1)} = c_{x,min} + j_1 \Delta c_x$, with $c_x^{(0)} = c_{x,min}$ and $c_x^{(J_1)} = c_{x,max}$. The velocities c_y and c_z are discretized accordingly; a discrete velocity $(c_x^{(j_1)}, c_y^{(j_2)}, c_z^{(j_3)})$ of the grid will be denoted by c_j, where $j = (j_1, j_2, j_3)$. Finally, we also choose a time discretization with $t_n = n\Delta t$.

Eqn. (17) is classically approximated by a finite volume scheme,

$$f_{i,j}^{n+1} = f_{i,j}^n - \frac{\Delta t}{\Delta x}(\mathcal{F}_{i+\frac{1}{2},j}^n - \mathcal{F}_{i-\frac{1}{2},j}^n) - \Delta t\, \nu_{i,j}^n (f_{i,j}^n - f_{\gamma,i,j}^n),$$

where the above quantities are defined as follows:

- $f_{i,j}^n$ is an approximation of $f\,(x_i, t_n, c_j)$.
- numerical fluxes are defined by

$$\mathcal{F}_{i+\frac{1}{2},j}^n = \frac{1}{2}\left(c_x^{(j_1)}(f_{i+1,j}^n + f_{i,j}^n) - |c_x^{(j_1)}|(\Delta f_{i+\frac{1}{2},j}^n - \Phi_{i+\frac{1}{2},j}^n) \right),$$

with the notation $\Delta f^n_{i+\frac{1}{2},j} = f^n_{i+1,j} - f^n_{i,j}$. The flux limiter function $\Phi^n_{i+\frac{1}{2},j}$ allows to obtain a second order scheme, e.g. $\Phi^n_{i+\frac{1}{2},j} = 0$ for first order, and $\Phi^n_{i+\frac{1}{2},j} = \text{minmod}(\Delta f^n_{i-\frac{1}{2},j}, \Delta f^n_{i+\frac{1}{2},j}, \Delta f^n_{i+\frac{3}{2},j})$ for second order;

- the collision frequency is defined by (see Eqn. (12))

$$\nu^n_{i,j} = \frac{\rho^n_i \frac{k}{m} T^n_i}{\mu(T^n_i)} \hat{\nu}(\eta^n_{i,j}), \qquad \text{with} \qquad \eta^n_{i,j} = \frac{\left((c_x^{(j_1)} - v^n_i)^2 + (c_y^{(j_2)})^2 + (c_z^{(j_3)})^2\right)^{\frac{1}{2}}}{\sqrt{2\frac{k}{m}T^n_i}};$$

- macroscopic quantities are defined as in Eqn. (1) where now continuous integrals are replaced by discrete sums on the velocity grid

$$\left(\rho^n_i,\ \rho^n_i v^n_i,\ \tfrac{3}{2}\rho^n_i \tfrac{k}{m} T^n_i\right) = m \sum_{j=(0,0,0)}^{(J_1,J_2,J_3)} \left(1,\ c_x^{(j_1)},\ C^2_{(j_1,j_2,j_3)}\right) f^n_{i,j}\, \Delta\mathbf{c},$$

with $C^2_{(j_1,j_2,j_3)} = \left((c_x^{(j_1)} - v^n_i)^2 + (c_y^{(j_2)})^2 + (c_z^{(j_3)})^2\right)$ and $\Delta\mathbf{c} = \Delta c_x \Delta c_y \Delta c_z$.

- the approximation of $f_\gamma(x_i, t_n, c_j)$ is defined by

$$f^n_{\gamma,i,j} = a^n_i \exp\left[-\Gamma^n_i C^2_{(j_1,j_2,j_3)} + \gamma^n_i (c_x^{(j_1)} - v^n_i)\right],$$

where the three coefficients $a_i, \Gamma^n_i, \gamma^n_i$ are solutions of the discrete version of Eqn. (3),

$$\sum_j \nu^n_{i,j} m (f^n_{i,j} - f^n_{\gamma,i,j})\, \Delta\mathbf{c} = 0\ ,$$

$$\sum_j \nu^n_{i,j} m c_x^{(j_1)} (f^n_{i,j} - f^n_{\gamma,i,j})\, \Delta\mathbf{c} = 0\ ,$$

$$\sum_j \nu^n_{i,j} \frac{m}{2} c_j^2 (f^n_{i,j} - f^n_{\gamma,i,j})\, \Delta\mathbf{c} = 0\ .$$

These equations are solved by a Newton algorithm. This approximation has already been used by Frezzotti in Ref. 16, and has been mathematically investigated by one of the authors in[10].

Owing to this last approximation, our scheme is perfectly conservative for density, momentum, and total energy. Moreover, the total (physical) entropy is increasing. The positivity

of the phase density is preserved if at each iteration the time step follows the condition

$$\Delta t \left(\max_{i,j} \nu^n_{i,j} + \max_j \frac{|c_x^{(j_1)}|}{\Delta x} \right) < 1 \ . \tag{18}$$

B Implicit scheme

The condition (18) poses a problem for computing dense or rapid regimes with the above numerical scheme, since for these Δt must be small and the convergence is very slow.

A classical way to overcome this difficulty is to use a linearized implicit scheme that can be viewed as relaxed-Newton algorithm for the steady equation,

$$f^{n+1}_{i,j} + \frac{\Delta t}{\Delta x}(\mathcal{F}^{n+1}_{i+\frac{1}{2},j} - \mathcal{F}^{n+1}_{i-\frac{1}{2},j}) + \Delta t\, \nu^n_{i,j}(f^{n+1}_{i,j} - f^{n+1}_{\gamma,i,j}) = f^n_{i,j} \ .$$

Since $f^{n+1}_{\gamma,i,j}$ is a non linear function of $f^{n+1}_{i,j}$, it is linearized as follows

$$f^{n+1}_{\gamma,i,j} \approx f^n_{\gamma,i,j} + [\mathcal{D}^n_i(f^{n+1}_i - f^n_i)]_j,$$

where $\mathcal{D}^n_i$ is the Jacobian of the mapping $g \mapsto f_\gamma[g]$ evaluated at f^n_i. For the second order scheme, the flux limiters (non differentiable) are kept explicit. The following δ matrix-form of the scheme is more adapted to computations

$$\left(\frac{I}{\Delta t} + T + R^n \right) \delta f^n = RHS^n, \tag{19}$$

where $\delta f^n = f^{n+1} - f^n$, I is the unit matrix, T is a matrix such that $(Tf^n)_{i,j} = \frac{1}{\Delta x}(\mathcal{F}^n_{i+\frac{1}{2},j} - \mathcal{F}^n_{i-\frac{1}{2},j})$ with only the first order fluxes, R^n is defined such that $(R^n f^n)_{i,j} = \nu^n_{i,j}(f^n_{i,j} - [\mathcal{D}^n_i f^n_i]_j)$, and

$$RHS^n_{i,j} = -\frac{1}{\Delta x}(\mathcal{F}^n_{i+\frac{1}{2},j} - \mathcal{F}^n_{i-\frac{1}{2},j}) - \nu^n_{i,j}(f^n_{i,j} - f^n_{\gamma,i,j}) \tag{20}$$

which contains the limiters for the second order scheme.

The scheme now reads as a linear system to be solved at each iteration. This can be done efficiently, and this method has been proved to be very fast for computing steady flows.

A similar scheme has been proposed by Frezzotti[16], but the main difference is that in his method, the equilibrium distribution is not implicit. It has been shown in Ref. 10 that the convergence of such a scheme is slower than ours.

C Remark on the velocity grid

The velocity grid is appropriately chosen for each case. Since the same grid is used in each space point, it should be large and precise enough to correctly describe the flow (*i.e.* the distributions everywhere in the space domain). Then the bounds are given by a combination between the maximum macroscopic velocity and temperature of the flow ($\max_x(v_x+a\sqrt{\frac{k}{m}T})$, where we take $a = 4$). The step of the grid is given by the smallest temperature (*i.e.* $\Delta\mathbf{c} = \min_x \sqrt{\frac{k}{m}T}$). These quantities can be estimated by the data, *e.g.* velocity and temperature at infinity and wall temperature (see Ref. 9 for other estimates). In the numerical tests of this article, the bounds of the grid are chosen as explained above, but the step of the grid is computed differently. In order to obtain very accurate comparisons between the models, the difference due to velocity discretization had to be eliminated. Consequently, the number of discrete velocities is taken so that an increase of this number by 10 points in each direction does not affect the results to a magnitude greater than 1%.

IV. NUMERICAL RESULTS

The linearized implicit scheme of second order is used in most of the subsequent computations, with a CFL number of 10000 (*i.e.* Δt is 10000 times the explicit time step). The criterion used to determine whether the flow has reached steady state is the reduction of the quadratic global residual $\frac{1}{\Delta t}(\sum_{i,j}|RHS^n_{i,j}|^2)^{\frac{1}{2}}$ by a factor of 10^5. In all results of this section gas-surface interactions are Maxwellian reflections with total accommodation, *i.e.* incident molecules are supposed to be re-emitted by the wall with a Maxwellian distribution $\rho_w M[1, u_w, T_w]$,where u_w is the wall velocity, and T_w is the wall temperature. The coefficient ρ_w is determined to ensure a zero mass flux normal to the wall. In our numerical scheme, the Maxwellian is naturally replaced by the discrete Maxwellian associated to u_w and T_w. Numerically, the boundary conditions (gas-surface, symmetry axes, etc.) are treated by a classical ghost cell technique.

A Couette flow at Kn = 0.01199

We consider one-dimensional plane Couette flow and use the same data as Bird in Ref. 14. The gas, argon, lies between two plates maintained at a temperature of $T_w = T_0 = 273$ K. One plate is at rest while the other is moving with the velocity $u_w = 300$ m/s in y direction, the distance between the plates is $L = 1$m. Initially the gas is at T_0, and its density is $\rho_0 = 9.28 \times 10^{-6}$ kg/m^3, corresponding to a pressure $p_0 = \rho_0 \frac{k}{m} T_0 = 0.528\,\mathrm{Pa}$. The viscosity of the gas is given by Eqn. (13) with $\mu_0 = 2.117 * 10^{-5} \frac{kg}{ms}$ and $\omega = 0.81$. For this data Bird obtains the Knudsen number for his variable hard sphere model as 0.00925, while one obtains $Kn = 0.01199$ from Eqn. (15).

For our calculations we use a grid of 200 cells in x direction and $40 \times 46 \times 40$ discrete velocities with bounds $[-980, 980] \times [-952, 1252] \times [-980, 980]$ (in m/s). With this velocity grid, a further increase of the number of grid points does not improve the results by a magnitude larger than 0.05%, except at the left boundary for the velocity that cannot be improved by more than 1%. Consequently, this discrete velocity grid can be considered as optimal.

For the given problem the total mass is physically conserved in time. Consequently, a conservative numerical method is essential in order to converge towards the correct steady state. As explained in the previous section, the choice of an appropriate iterative solver is crucial. For instance a classical Gauss-Seidel method is non-conservative, and this leads to a steady-state which is correct for temperature and velocities, but not for the density. In this paper, we use a simple correction of the distribution function at each time step by a factor equal to the initial total mass divided by the current total mass. This is sufficient to recover the correct steady state conditions.

Figures 3-7 show profiles for the following models : DSMC with variable hard sphere model (we use the code and data provided with the floppy disk of Ref. 14, also available on the web at `http://www.gab.com.au/`), the standard BGK model, the ES-BGK model, and the velocity-dependent collision frequency BGK models $\hat{\nu}_1(\eta), \hat{\nu}_2(\eta), \hat{\nu}_3(\eta)$ introduced in

Section II E (from now on referred to as $\nu\,(C)$-BGK models). The collision frequency $\hat{\nu}_4\,(\eta)$ is not considered, since its maximum value is so large that the matrix of the linear system (19) is very ill-conditioned. Our linear solver is then not efficient enough to solve the linear system and our method breaks down.

Moreover, we do not show any results obtained with the discontinuous model $\hat{\nu}_5\,(\eta)$. While this model gives good results at low Knudsen numbers, tests that we ran at larger Knudsen numbers revealed unphysical steps in the curves and we decided to not further study this particular model.

For Knudsen numbers below $\sim$0.01 we are in the continuum regime where the flow is expected to be well described by the Navier-Stokes-Fourier equations. Here it must be noted that all BGK models considered, but not the standard BGK, are constructed such that they have the same viscosity and heat conductivity in the continuum regime. Thus, in the simulation of this problem, we expect only small differences between the improved BGK models, but marked differences to the results from standard BGK.

Indeed, for density and temperature profiles, Figs. 3 and 4, we observe that the results obtained with the standard BGK model are quite different from the others. All modified BGK models are very close to each other, and very close to the DSMC results. The strong differences between standard BGK and the improved ones are related to the Prandtl number while the smaller differences between DSMC, ES-BGK, and $\nu\,(C)$-BGK, are due to Knudsen number effects and nonlinearities. However, the velocity is independent of the Prandtl number, and all models give the expected straight line, see Fig. 5. For heat flux and shear stress curves, there is a significant statistical scatter in the DSMC results, and we can just note that the all models are quite close (Figs. 6, 7).

Following Bird[14] further, we next consider the same case with a higher wall velocity of 1000 m/s. The results are plotted in Figures 8-12. Now the statistical scatter of the DSMC results is very small. Again we note that the standard BGK model does not agree with the DSMC calculations due to the wrong Prandtl number, while the results obtained with the ES-BGK and $\nu\,(C)$-BGK models are very close to DSMC. Indeed, no marked differences

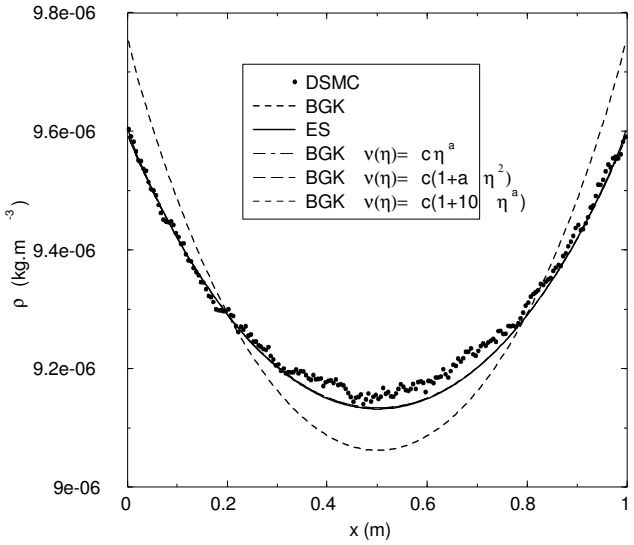

FIG. 2: Couette flow. Density profiles for $u_w = 300$ m/s and Kn $= 0.01199$.

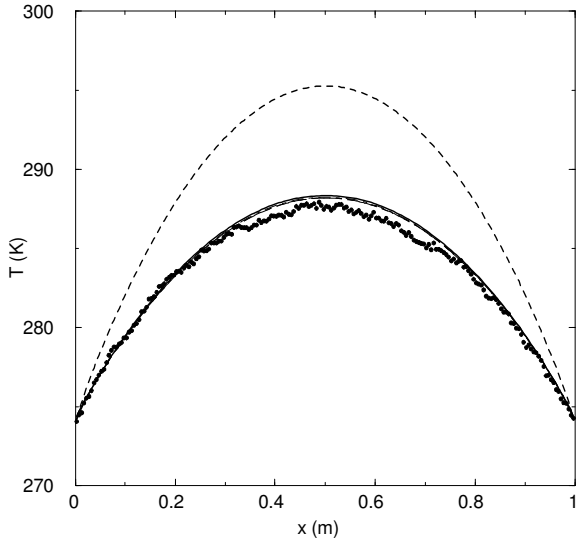

FIG. 3: Couette flow. Temperature profiles for $u_w = 300$ m/s and Kn $= 0.01199$.

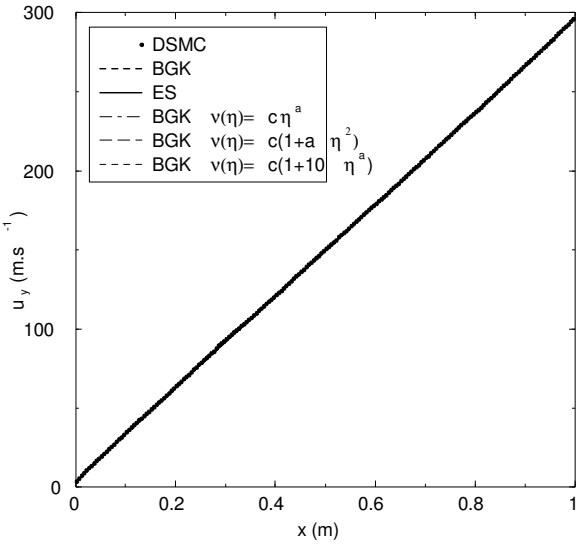

FIG. 4: Couette flow. Velocity profile for $u_w = 300$ m/s and Kn $= 0.01199$.

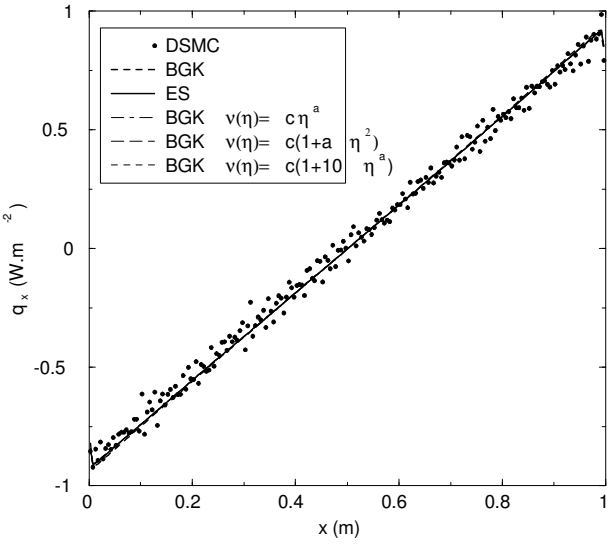

FIG. 5: Couette flow. Heat flux profiles for $u_w = 300$ m/s and Kn $= 0.01199$.

between the results can be observed. The DSMC results for heat flux and shear stress are more affected by statistical noise, and the results from ES-BGK and $\nu\,(C)$-BGK models lie within the error margin.

At this small Knudsen number, the BGK results should agree well with solutions of the Navier-Stokes-Fourier equations, and this allows us to compute viscosity, heat conductivity and the Prandtl number from our results. Viscosity and heat conductivity are computed from Eqs. (9) as the ratio between viscous stress and velocity gradient, and heat flux and temperature gradient, respectively. The results for the various BGK models are shown in Figs. 12 and 13; the DSMC results exhibit too much noise that no meaningful data is obtained for the velocity gradient. From the pictures, it becomes clear that all BGK models with correct Prandtl number yield identical results, while the original BGK model exhibits different results. The curves are best understood by recalling Eqn. (13), which gives the temperature difference of the viscosity. The spatial variation of the viscosity is due to the variation in temperature, and the higher viscosity values for the BGK model reflect the higher temperatures for that model. These, in fact, are observed since the standard BGK model underestimates the heat conductivity (= larger Prandtl number), so that the heat of friction is not removed as efficient as for a gas with proper Prandtl number. The low value of heat conductivity can also be seen in Fig. 13, where all BGK models with correct Prandtl number give the same values. The computation of the Prandtl number from viscosity and heat conductivity yields only marginal variation over the space variable, and the following mean values were found: BGK: Pr = 1.02811, ES-BGK: Pr = 0.67641, BGK-ν_1: Pr = 0.67960 , BGK-ν_2: Pr = 0.67538, BGK-ν_3: Pr = 0.67535 . The Prandtl number is sufficiently close to its proper value of 2/3 for all but the standard BGK model. The small deviations from the proper value are likely due to Knudsen number effects, which also are reflected in the boundary layers and jumps at the boundaries (in order to exclude Knudsen layer effects, we averaged only over the inner 80% of the curves).

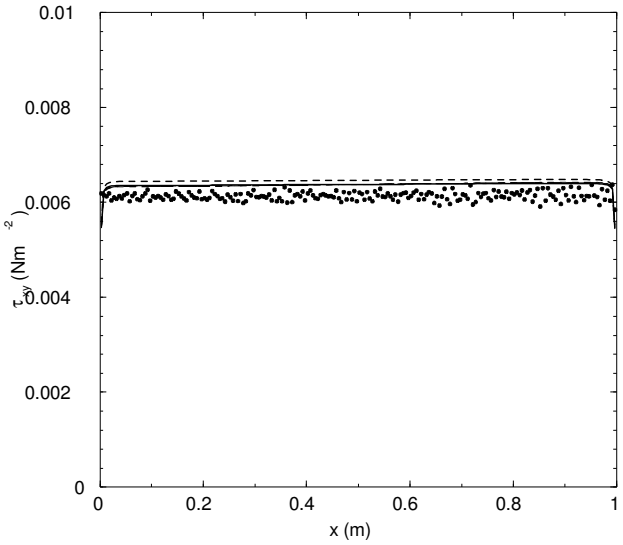

FIG. 6: Couette flow. Shear stress profiles for $u_w = 300$ m/s and Kn $= 0.01199$.

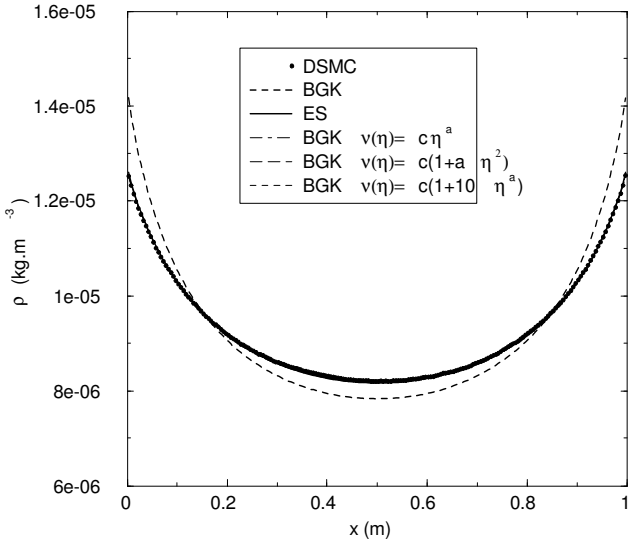

FIG. 7: Couette flow. Density profiles for $u_w = 1000$ m/s and Kn $= 0.01199$.

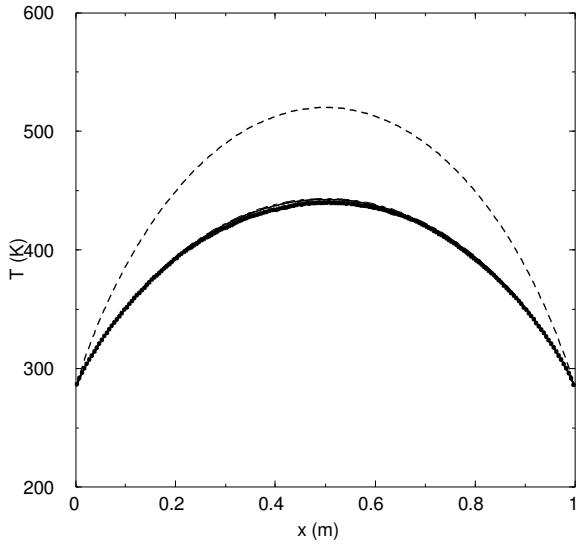

FIG. 8: Couette flow. Temperature profiles for $u_w = 1000$ m/s and Kn $= 0.01199$.

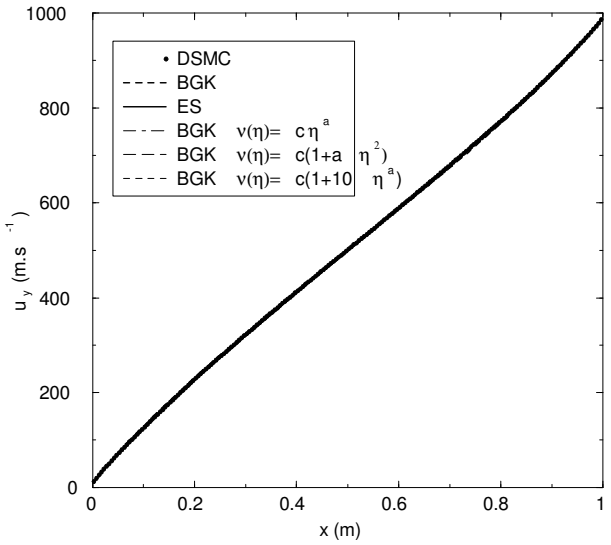

FIG. 9: Couette flow. Velocity profile for $u_w = 1000$ m/s and Kn $= 0.01199$.

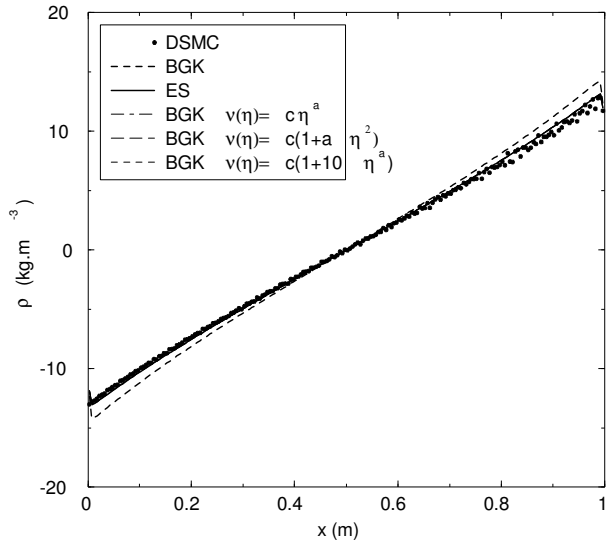

FIG. 10: Couette flow. Heat flux profiles for $u_w = 1000$ m/s and Kn $= 0.01199$.

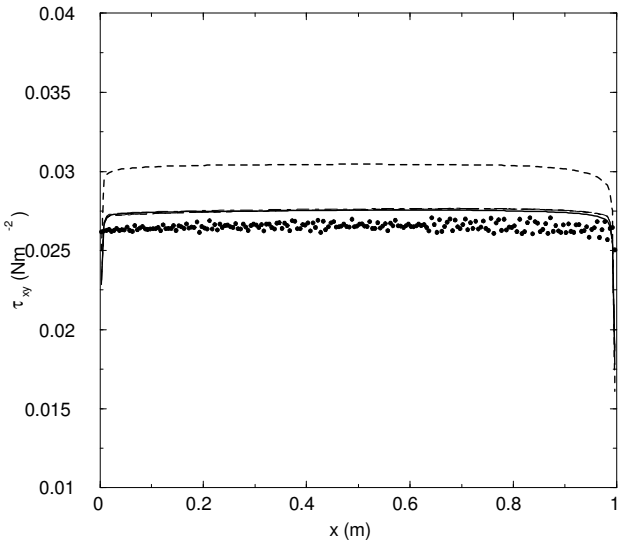

FIG. 11: Couette flow. Shear stress profiles for $u_w = 1000$ m/s and Kn $= 0.01199$.

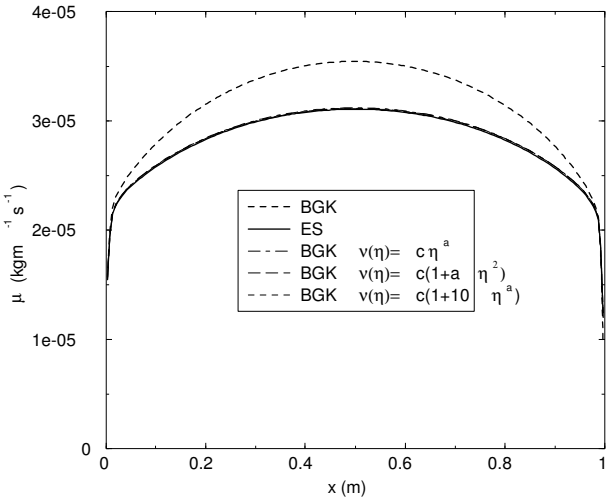

FIG. 12: Viscosity for the various models computed from the numerical solutions of the BGK models via the Navier-Stokes law, Kn = 0.1199, $u_w = 1000$ m/s .

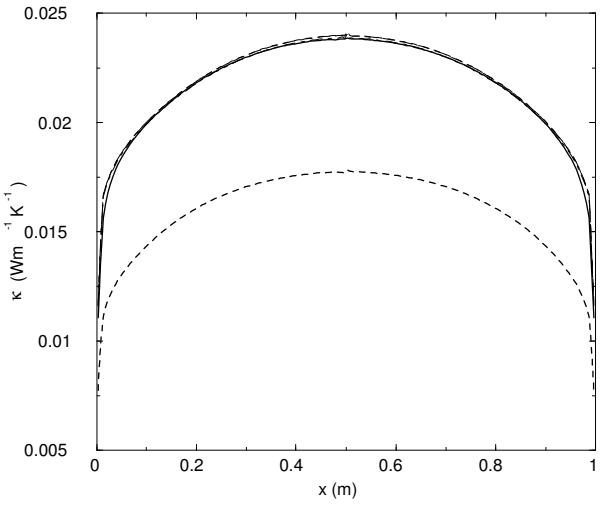

FIG. 13: Heat conductivity for the various models computed from the numerical solutions of the BGK models via Fourier's law, at Kn = 0.1199, $u_w = 1000$ m/s.

B Couette flow at Kn = 0.1199

Next we consider slow and fast Couette flow with a density of 9.28×10^{-7} kg/m^3, corresponding to a Knudsen number of $Kn = 0.1199$, so that the Knudsen number is ten times larger as for the first test. For the calculation we use $50 \times 56 \times 50$ discrete velocities with bounds $[-990, 990] \times [-950, 1267] \times [-990, 990]$ for the low-speed case, and $50 \times 59 \times 50$ discrete velocities with bounds $[-1300, 1300] \times [-1040, 2028] \times [-1300, 1300]$ for the high-speed case. For the same reasons as above, these grids can be considered to be optimal.

The results are plotted in Figures 13-18 for the wall velocity $u_w = 300$ m/s and in figures 19-24 for the wall velocity $u_w = 1000$ m/s.

For Knudsen numbers between 10 and 0.01 we are in the transition regime, where Knudsen number effects are expected to be clearly visible. These include, but are not limited to, jumps in temperature and velocity at the walls, and Knudsen boundary layers.

For the low-speed flow, Figs. 13-18, it appears that the standard BGK model gives marked deviations again, while the ES-BGK model gives results very close to the DSMC calculations. The $\nu(C)$-BGK models exhibit visible deviations in the profiles for density, and temperature. In particular, the temperature jumps at the boundaries are met best by the standard BGK, and the ES-BGK model. The same behavior is observed for velocity slip, see Fig. 16 for a close-up.

While all models agree on the heat flux (Fig. 17), some differences can be seen in the shear stress (Fig. 18), where the two last $\nu(C)$-BGK models give the best agreement with DSMC.

For the high-speed flow, Figs. 19-24, we observe just the same: The ES-BGK model yields results in close agreement to the DSMC calculations, while the $\nu(C)$-BGK models show marked deviations, which are, in some cases (e.g. density) of the same order as the deviations of the standard BGK model.

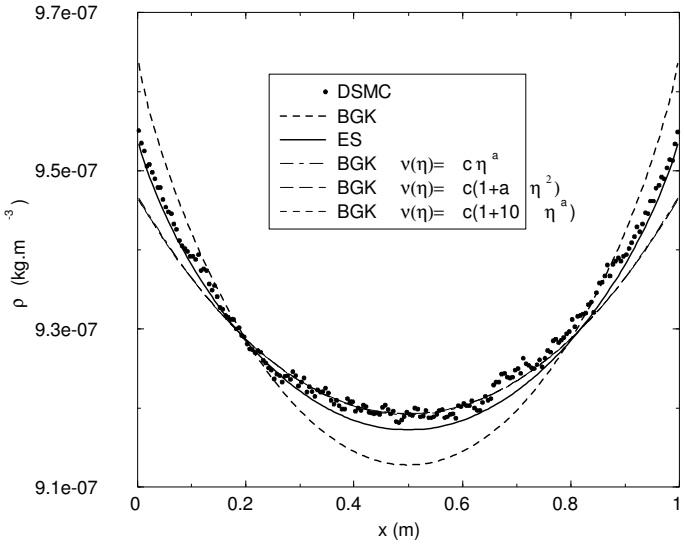

FIG. 14: Couette flow. Density profiles for $u_w = 300$ m/s and Kn $= 0.1199$.

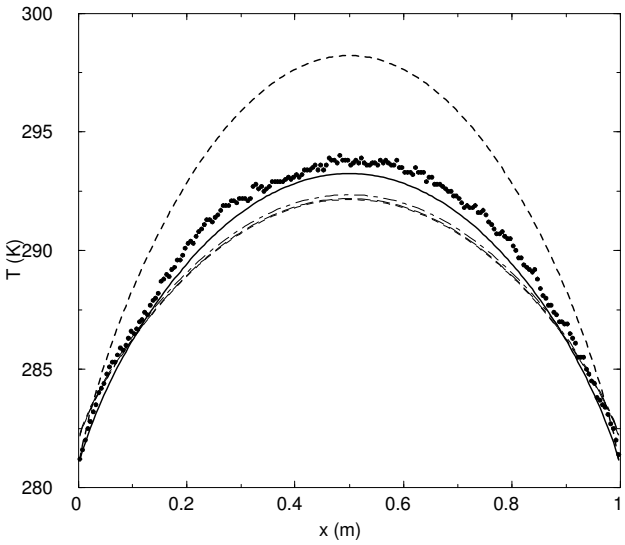

FIG. 15: Couette flow. Temperature profiles for $u_w = 300$ m/s and Kn $= 0.1199$.

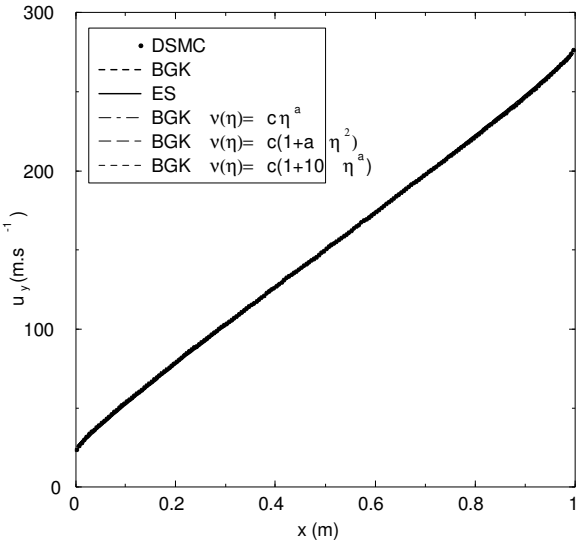

FIG. 16: Couette flow. Velocity profile for $u_w = 300$ m/s and Kn $= 0.1199$.

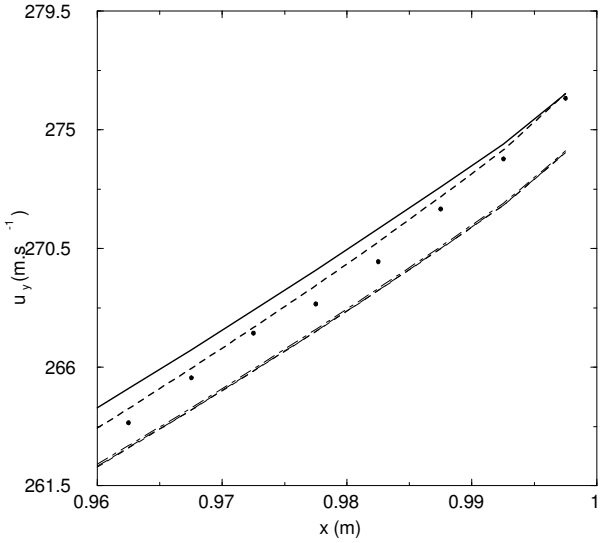

FIG. 17: Couette flow. Velocity profile zoom for $u_w = 300$ m/s and Kn $= 0.1199$.

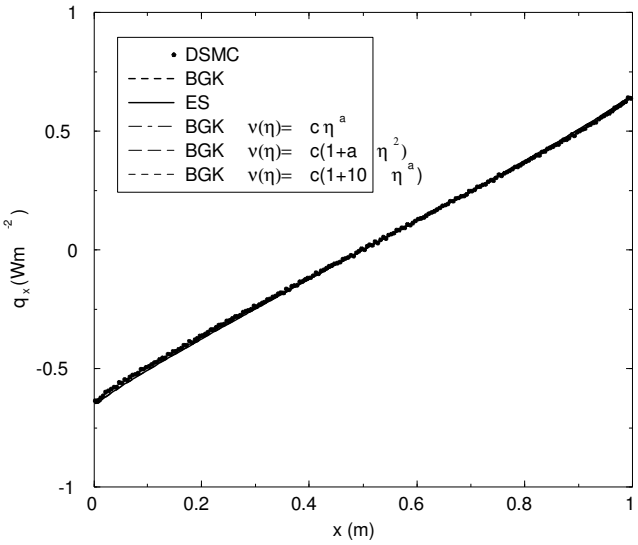

FIG. 18: Couette flow. Heat flux profiles for $u_w = 300$ m/s and Kn $= 0.1199$.

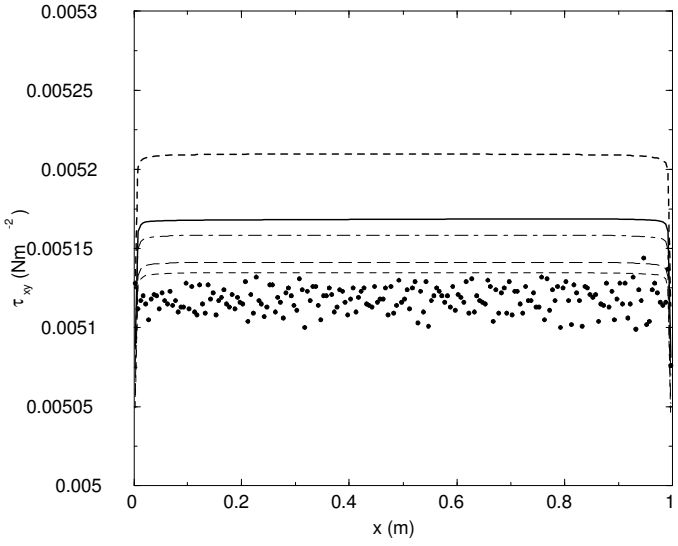

FIG. 19: Couette flow. Shear stress profiles for $u_w = 300$ m/s and Kn $= 0.1199$.

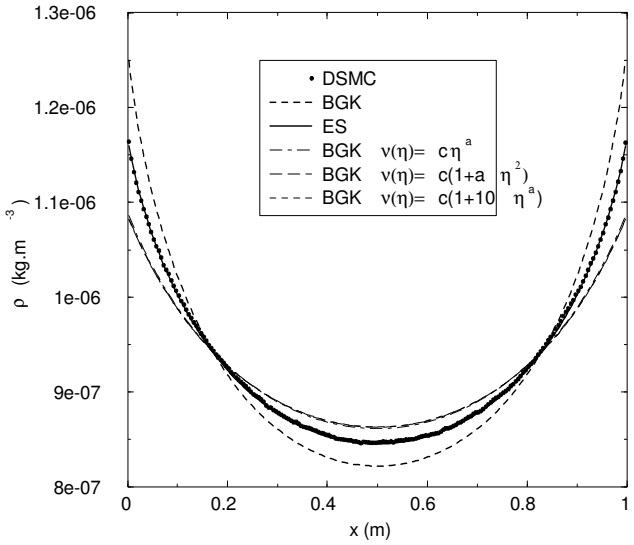

FIG. 20: Couette flow. Density profiles for $u_w = 1000$ m/s and Kn $= 0.1199$.

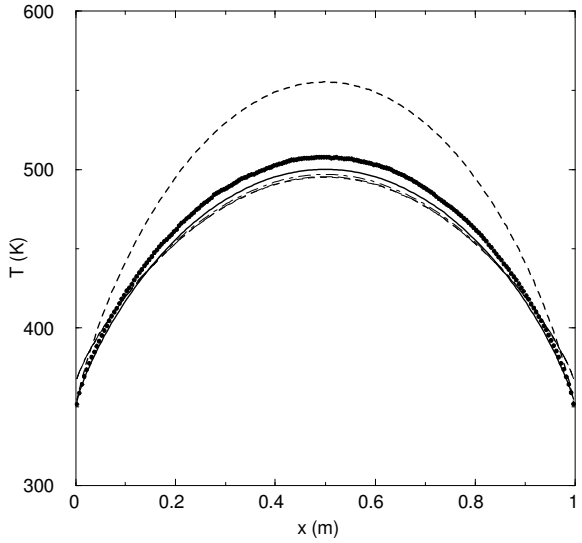

FIG. 21: Couette flow. Temperature profiles for $u_w = 1000$ m/s and Kn $= 0.1199$.

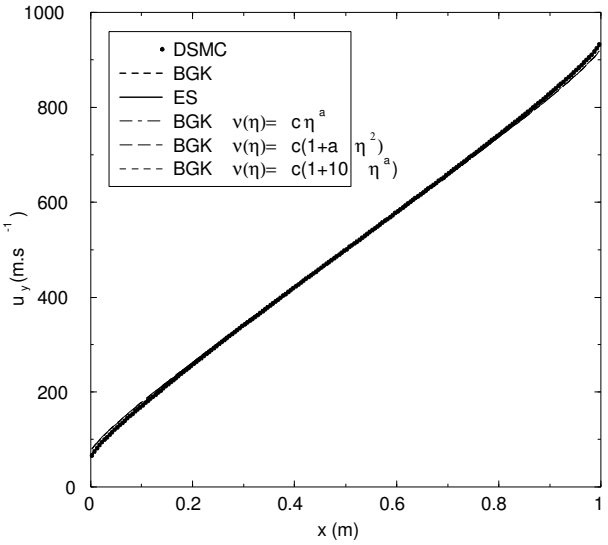

FIG. 22: Couette flow. Velocity profile for $u_w = 1000$ m/s and Kn $= 0.1199$.

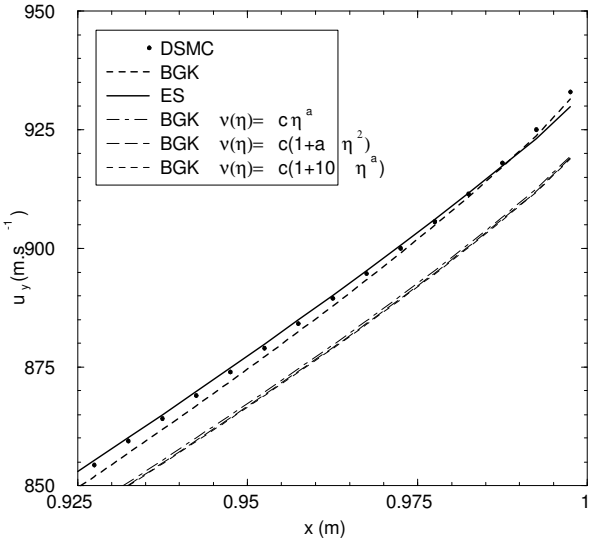

FIG. 23: Couette flow. Velocity profile zoom for $u_w = 1000$ m/s and Kn $= 0.1199$.

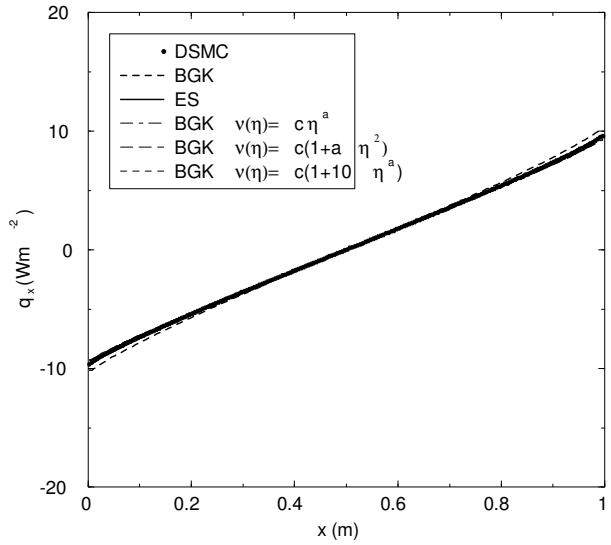

FIG. 24: Couette flow. Heat flux profiles for $u_w = 1000$ m/s and Kn $= 0.1199$.

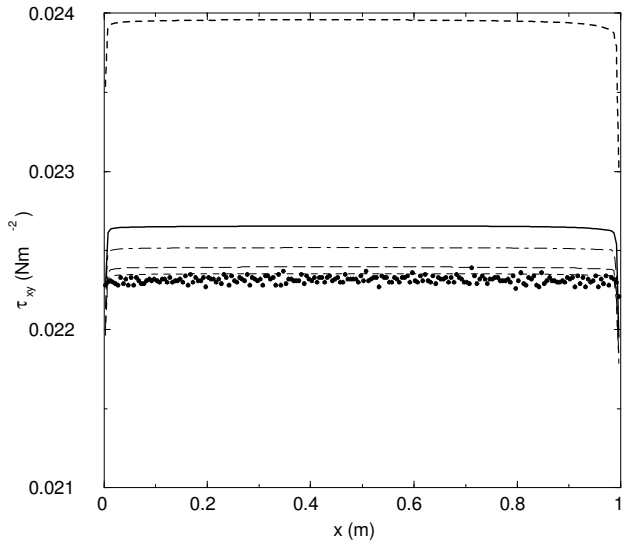

FIG. 25: Couette flow. Shear stress profiles for $u_w = 1000$ m/s and Kn $= 0.1199$.

C Couette flow at Kn = 1.199

We now consider fast and slow Couette flow at an even higher Knudsen number of Kn = 1.199 (density of 9.28×10^{-8} kg/m^3), so that the Knudsen number is hundred times larger as for the first test. Now, we use $50 \times 54 \times 50$ discrete velocities with bounds $[-1009, 1009] \times [-928, 1251] \times [-1009, 1009]$ for the low-speed case, and $60 \times 67 \times 60$ discrete velocities with bounds $[-1463, 1463] \times [-1121, 2145] \times [-1463, 1463]$ for the high-speed case. Again, these grids can be considered to be optimal. Note that the large number of points is necessary due to the rarefied regime: The collisions are not numerous enough to prevent the half-space Maxwellians at the walls from propagating into the domain. Consequently, the distribution has very strong gradients that must be captured by the grid. If this is not taken into account, macroscopic quantities can be seriously affected, see Ref. 17.

The results are plotted in Figs. 25-27 for $u_w = 300$ m/s and in Figs. 28-31 for $u_w = 1000$ m/s. For both cases, we present only the profiles for density, temperature, and velocity.

It is obvious that all models fail to match the DSMC simulations at this large Knudsen number. Still the best agreement can be found from the ES-BGK model, but also here the deviations are obvious. The curves obtained with the $\nu\,(C)$-BGK models are very flat,and the density profiles are even inverted for the fast flow case, see Figs. 28-29.

Also we observe that the standard BGK model can compete with the other models at this flow conditions. Indeed, the standard BGK matches the DSMC temperature and velocity curves best of all models.

D A remark on Knudsen numbers

We believe that the above results can be understood as follows: Under the given flow conditions the mean free path is of the order of the wall distance. Hence, Knudsen number effects become important, if not dominant. Since the Knudsen number of the standard BGK model agrees well with the Knudsen number of the DSMC calculations, the approximate

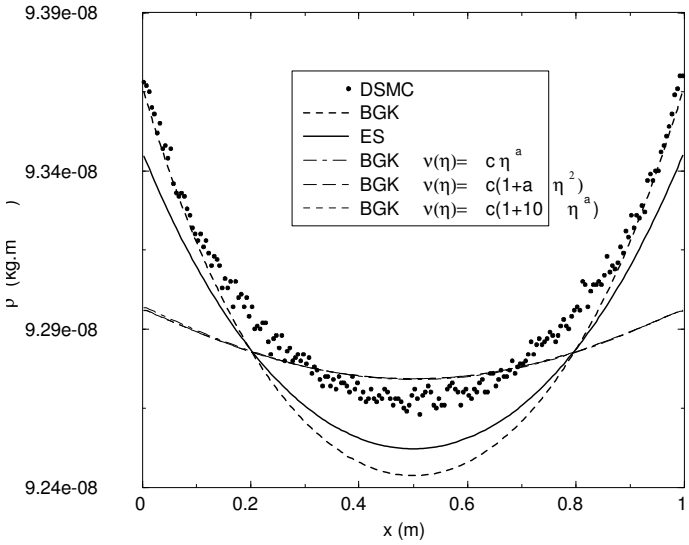

FIG. 26: Couette flow. Density profiles for $u_w = 300$ m/s and Kn = 1.199.

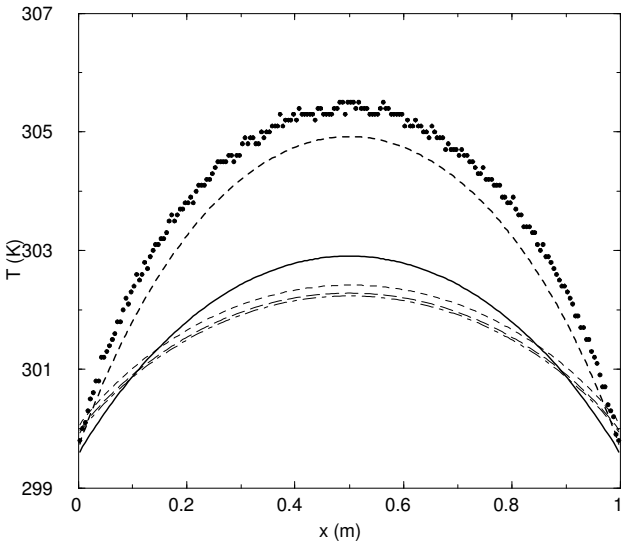

FIG. 27: Couette flow. Temperature profiles for $u_w = 300$ m/s and Kn = 1.199.

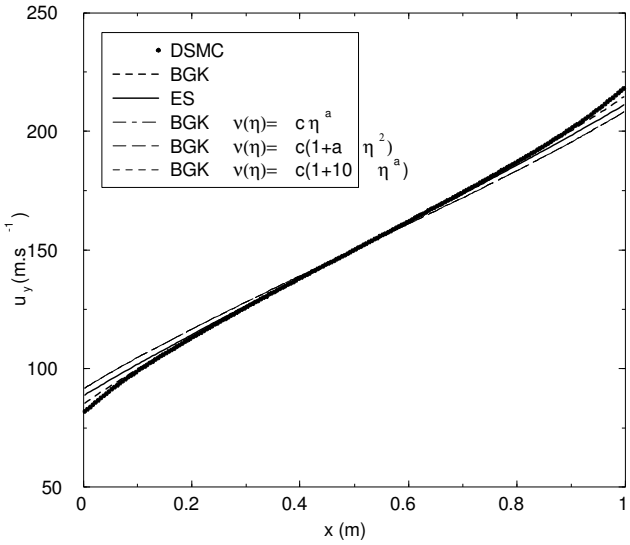

FIG. 28: Couette flow. Velocity profiles for $u_w = 300$ m/s and Kn = 1.199.

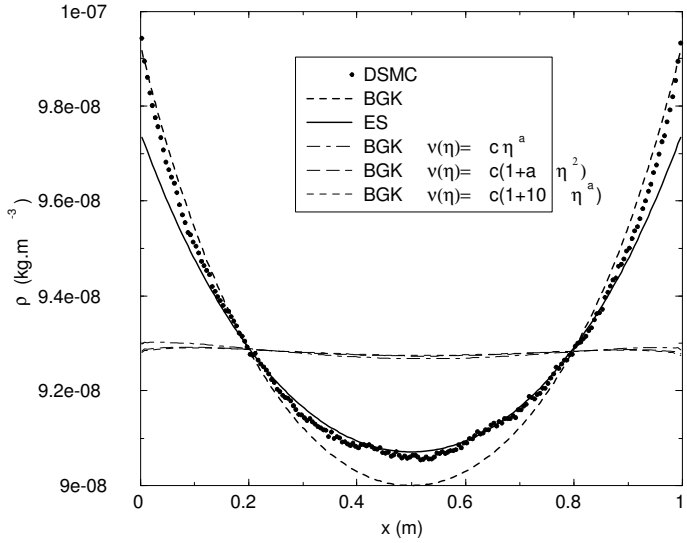

FIG. 29: Couette flow. Density profiles for $u_w = 1000$ m/s and Kn = 1.199.

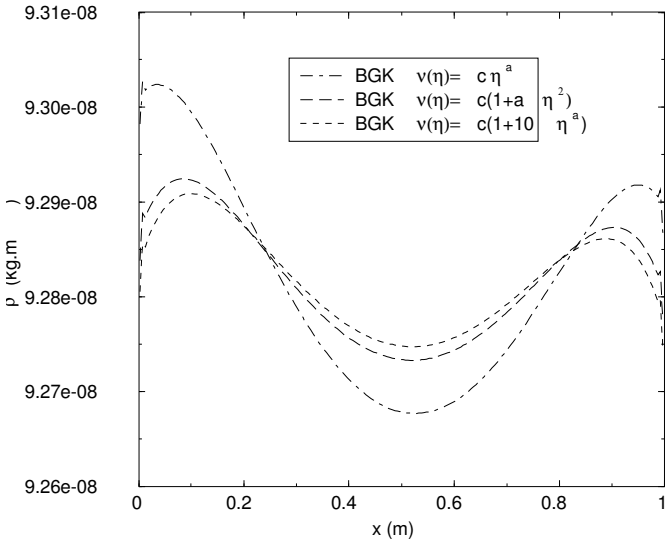

FIG. 30: Couette flow. Density profiles for $u_w = 1000$ m/s and Kn $= 1.199$. New scale for the $\nu\,(C)$-BGK models.

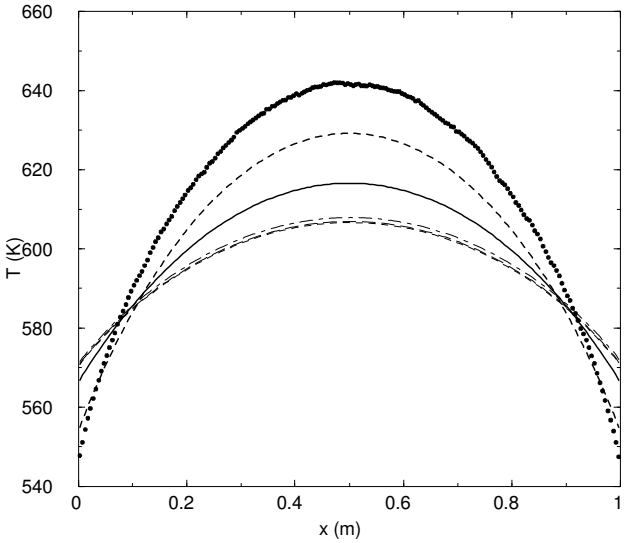

FIG. 31: Couette flow. Temperature profiles for $u_w = 1000$ m/s and Kn $= 1.199$.

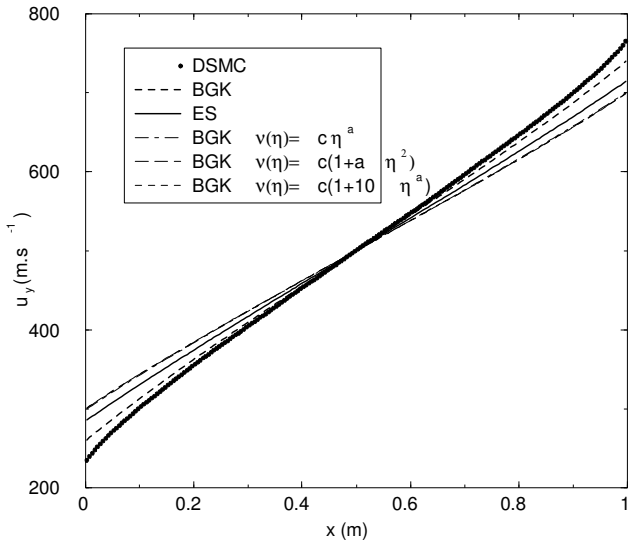

FIG. 32: Couette flow. Velocity profiles for $u_w = 1000$ m/s and Kn $= 1.199$.

agreement between both should not be a surprise. A similar argument holds for the ES-BGK model. Note that all models were constructed such that they have the same Knudsen number Kn as defined in Eqn. (15). However, their mean free paths $\bar{\lambda}$ and the corresponding Knudsen numbers $\overline{\text{Kn}}$ as given in Eqn. (16) differ. Thus the Knudsen number $\overline{\text{Kn}}$ of the standard BGK and the ES-BGK model are by a factors $\chi_{BGK}/\chi_{DSMC} = 1.65$ and $\chi_{ES-BGK}/\chi_{DSMC} = 2.475$ larger than that of the DSMC simulations. Thus, it needs to be checked, whether this difference accounts for some of the disagreement observed in the curves..

One might also guess, that the marked deviation of the $\nu\,(C)$-BGK models could be explained through the differences in the Knudsen numbers as well. Indeed, the Knudsen number $\overline{\text{Kn}}$ of these models is by a factor $\chi_1/\chi_{DSMC} = 3.63$ larger than the Knudsen number of the DSMC calculations. Larger Knudsen numbers correspond to flatter profiles, and this explains why the $\nu\,(C)$-BGK models give the flattest profiles, while BGK and ES-BGK models give profiles that are less flat than the DSMC calculations.

In order to learn more about the influence of the Knudsen number, we run a test where we used the same Knudsen numbers $\overline{\text{Kn}}$ for all models in the low velocity case. For this, we

chose the Knudsen numbers as

$$\mathrm{Kn}_\alpha = \frac{1}{\chi_\alpha}\overline{\mathrm{Kn}} = \frac{\chi_{DSMC}}{\chi_\alpha}\mathrm{Kn}_{DSMC}$$

where $\mathrm{Kn}_{DSMC} = 1.199$ is the Knudsen number for the DSMC calculations, and the values for χ_α can be found in the table below Eqn. (16). Thus, for this test, all models have the same mean free path based Knudsen number $\overline{\mathrm{Kn}} = 0.925$, corresponding to

$$\mathrm{Kn}_{BGK} = 0.72677 \quad , \quad \mathrm{Kn}_{ES-BGK} = 0.48451$$

$$\mathrm{Kn}_{\nu_1} = 0.330309 \quad , \quad \mathrm{Kn}_{\nu_2} = 0.331995 \quad , \quad \mathrm{Kn}_{\nu_2} = 0.331356$$

Figs. 33 - 35 show the corresponding profiles for density and temperature. Here, we see the interesting result that the shape of the profiles is quite similar for all models, while the jumps in temperature and velocity (slip) are differ notably between DSMC, standard BGK, ES-BGK, and the $\nu\,(C)$-BGK models. This stands in contrast to the results shown in Figs. 26-28, where all models exhibit jumps of similar size, but quite different shapes of the profiles.

These findings indicate that neither of the two Knudsen numbers - Eqs. (15) and (16) - is sufficient to characterize the flow. Indeed, the mean free path of an individual particle depends on the velocity, and it should not be surprising that this dependence cannot be captured by one mean value alone. As a direct conclusion follows that the simulation of gas flows at high Knudsen number with a kinetic model, e.g. variants of the BGK model, will be in better agreement with solutions of the Boltzmann equation (e.g. DSMC) when the collision frequency used in the kinetic models mimics the velocity dependence of the actual collision frequency.

E Stationary shock wave

As a second test case we consider the shock structure for a one-dimensional steady shock with upstream Mach numbers 1.4, 3 and 8 in argon, another of the reference problems

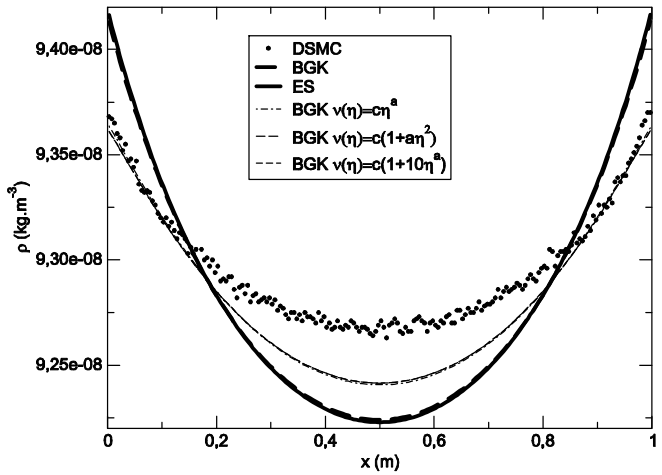

FIG. 33: Couette flow. Density profiles for $u_w = 300$ m/s and mean free path based Knudsen number $\overline{\mathrm{Kn}} = 0.925$.

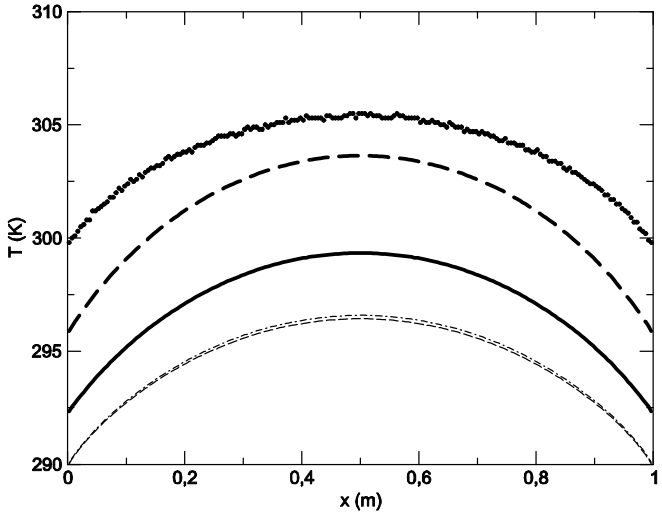

FIG. 34: Couette flow. Temperature profiles for $u_w = 300$ m/s and mean free path based Knudsen number $\overline{\mathrm{Kn}} = 0.925$.

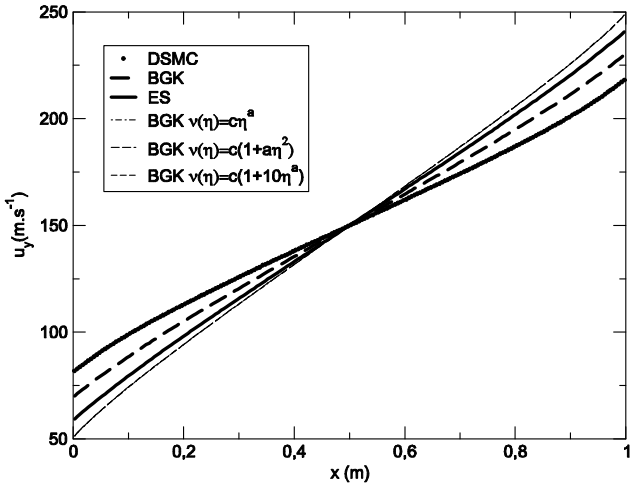

FIG. 35: Couette flow. Velocity profiles for $u_w = 300$ m/s and mean free path based Knudsen number $\overline{\mathrm{Kn}} = 0.925$.

in[14]. The details of the shock structure depend strongly on the details of the microscopic interaction, which are reflected in the velocity dependence of the collision frequency.

Because there is no fixed coordinate label for the shock profile inherent to the problem, it is possible that each computation yields a different shock position. In order to make a fair comparison, we therefore choose a new coordinate label x' such that $x' = 0$ corresponds to the "equal area point" x^* for density. It is defined by the following relation between total mass and densities ρ_L, ρ_R at left and right boundaries x_L, x_R of the computational domain

$$\int_{x_L}^{x^*} (\rho(x) - \rho_L)\, dx = \int_{x^*}^{x_R} (\rho_R - \rho(x))\, dx$$

We use a grid of 300 cells in x-direction, while the numbers of discrete velocity as well as the velocity bounds vary with the chosen Mach number. In particular we chose:

Mach 1.4 : 10x10x10 velocities, bounds [-871,1457]x[-1160,1160]x[-1160,1160]

Mach 3 : 16x16x16 velocities, bounds [-1571,2325]x[-1892,1892]x[-1892,1892]

Mach 5 : 24x24x24 velocities, bounds [-2463,3161]x[-2914,2914]x[-2914,2914]

Mach 8 : 38x36x36 velocities, bounds [-3844,5646]x[-4531,4531]x[-4531,4531]

These velocity grids are optimal in the sense explained in Section IV A.

The following figures show, for the various models, and Mach numbers, the profiles of relative density $\hat{\rho}$ and relative temperature $\hat{T}$, which are defined as

$$\hat{\rho} = \frac{\rho - \rho_L}{\rho_R - \rho_L} \quad , \quad \hat{T} = \frac{T - T_L}{T_R - T_L} \quad .$$

While all models give results of the same order of magnitude, the details of the shock profiles, as the Mach number increases, become very different in detail. These differences are only small at Mach number $Ma = 1.4$ (Figures 36 and 37), and one can say that all models agree reasonably well with the DSMC calculations.

As the Mach number increases to $Ma = 3$ (Figures 38 and 39), and $Ma = 8$ (Figures 40 and 41), the different kinetic models behave quite differently. These differences can be seen in both, density and temperature profiles, but are more marked in the temperature profile. Note the small slope of BGK and ES-BGK model to the left, where the $\nu(C)$-BGK models display almost a kink.

We believe that these differences can be well explained with the different velocity dependence of the collision frequency ν. For the standard BGK, and the ES-BGK models, the collision frequency is a constant, while the VHS (hard sphere) model used in the DSMC simulations assumes a velocity dependent collision frequency (see Figure 1), where fast particles collide more often. The $\nu(C)-$BGK models also have a velocity dependent collision frequency, which considerably overestimates the actual collision frequency of the hard spheres, as discussed in Section II.E.

Particles flying from the left into the shock are faster at higher Mach numbers, and the more collisions they have, the sooner they are deaccelerated. Thus, a theory with a velocity dependent collision frequency will lead to a steeper profile on the left, since fast particles travelling into the shock collide more often than the average.

This matches well with the results depicted in Figs. 36-41: Profiles for the models with constant collision frequency (BGK, ES-BGK), are flattest, while those for the models with the strongest dependence on velocity ($\nu(C)-$BGK models) are steepest. The steepness of

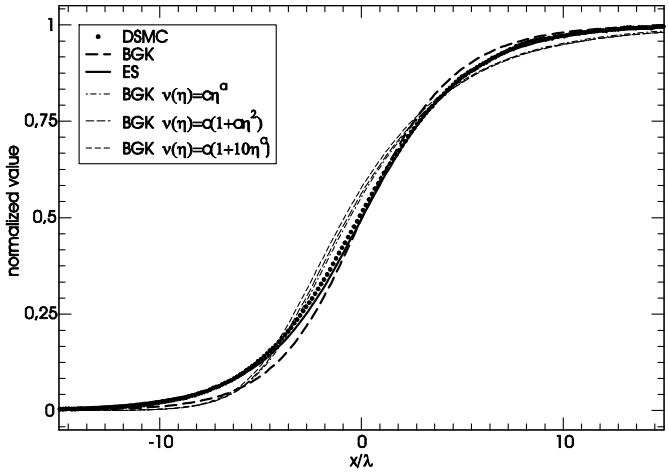

FIG. 36: Density profiles for shock at Mach number $Ma = 1.4$.

the DSMC curves, which are considered as our benchmark, lies in the middle between those of the BGK, and $\nu\,(C)$ −BGK models.

While none of the models can be considered best, one might argue that the ES-BGK agrees best in some smaller features, including an overshoot in the temperature curve, that is also observed in the DSMC curve.

V. CONCLUSIONS

From our results on Couette flow and shock structures, we can draw the following conclusions:

- In the continuum regime (Kn $\lesssim 0.01$) all BGK models with correct viscosity and heat conductivity, that is $\nu\,(C)$-BGK and ES-BGK models, give identical results that stand in good agreement with DSMC simulations and the Navier-Stokes-Fourier equations. Here, the $\nu\,(C)$-BGK model is in disadvantage to the ES-BGK model, since it requires a smaller time step. This can be seen from Eqn. (18) which relates the time step to the maximum value of the collision frequency. The maximum value $\nu\,(C_{\max})$ of the $\nu\,(C)$-BGK models are larger than the constant collision frequency of the ES-BGK model,

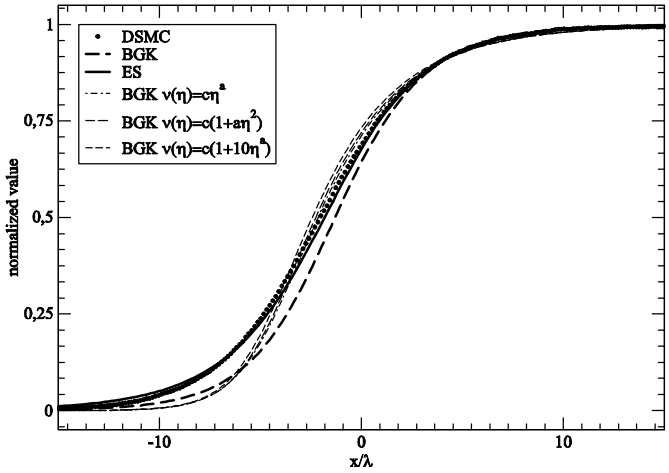

FIG. 37: Temperature profiles for shock at Mach number $Ma = 1.4$.

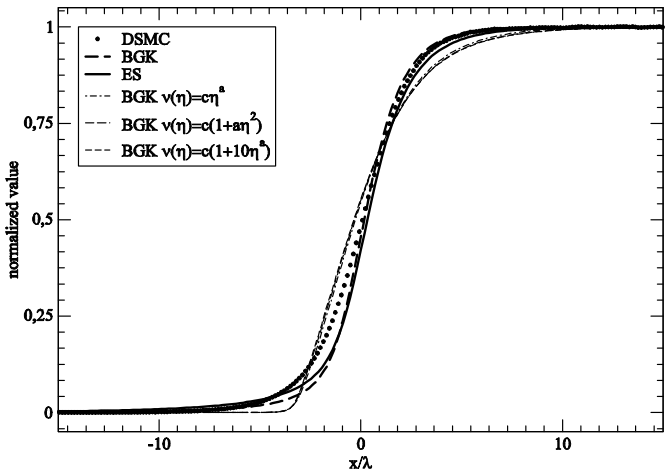

FIG. 38: Density profiles for shock at Mach number $Ma = 3$.

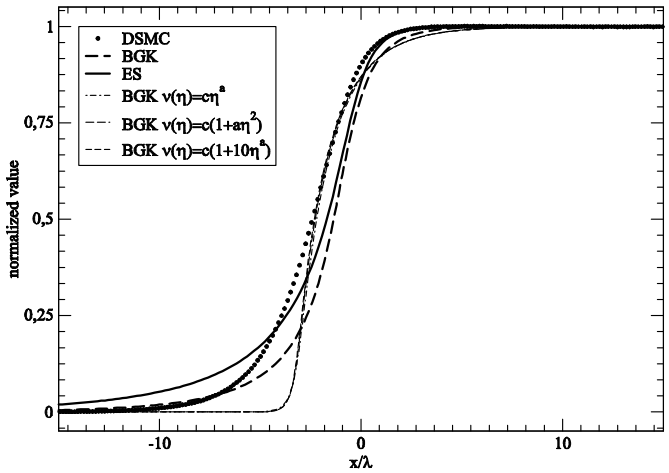

FIG. 39: Temperature profiles for shock at Mach number $Ma = 3$.

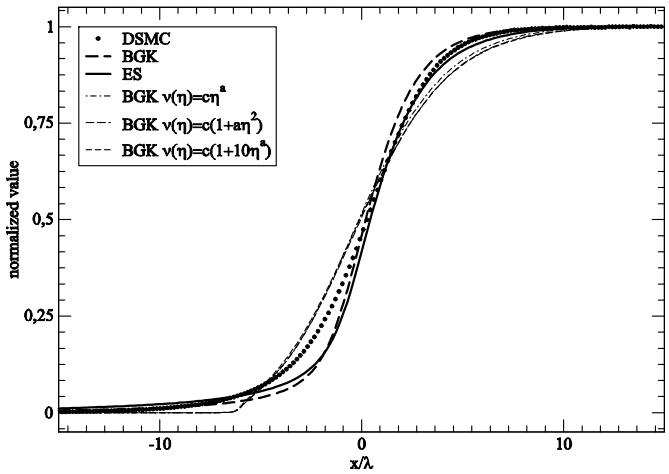

FIG. 40: Density profiles for shock at Mach number $Ma = 8$.

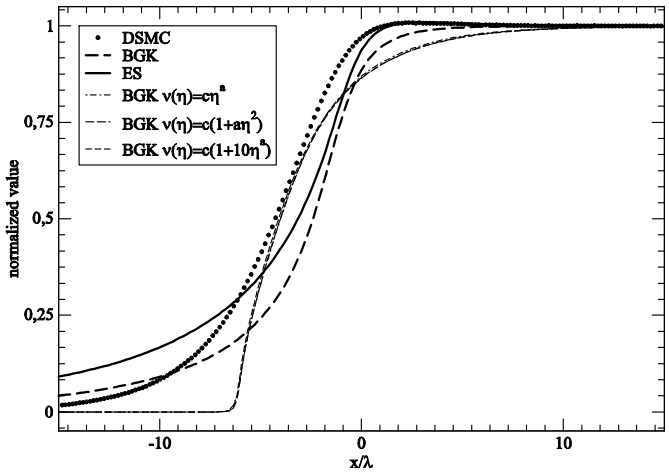

FIG. 41: Temperature profiles for shock at Mach number $Ma = 8$.

so that the latter allows larger time steps, and therefore faster numerical calculations. This is not a crucial issue for steady computations if implicit schemes are used, but this can be prohibitive for unsteady computations in which explicit schemes are generally used.

- When microscale effects become important, i.e. at Knudsen numbers above 0.01, all BGK-type models considered in this paper lead to different results. None of the models can be singled out as giving excellent results, since all differ from the DSMC simulations. The ES-BGK model is numerically cheapest, and we can say that it gives the best overall performance of the models considered.

- Altogether, our results show that improved BGK models are accurate in the continuum regime, and can give qualitatively good results in the transition regime. However, they are not capable of an accurate description of flows at large Knudsen numbers, and of shock structures. We believe that the reason for this failure lies in the insufficient description of the microscopic interaction dynamics which are represented by the collision frequency (or the mean free path).

Nevertheless, our results indicate that considering the non-isotropic Gaussian in the ES-BGK model, as well as considering velocity dependent collision frequencies in the $\nu(c)$-BGK models lead to considerable improvement over the standard BGK model. We expect that the combination of an anisotropic Gaussian with a velocity dependent collision frequency in a $\nu(C)$-ES-BGK model might give the best results. In such a model, one could use the physical collision frequency, e.g. Eqn. (11), so that the gas behavior is better described on the microscopic level. The $\nu(C)$-ES-BGK model will be considered in a future paper.

Acknowledgment: This research was supported by the Natural Sciences and Engineering Research Council (NSERC).

REFERENCES

[1] P.L. Bhatnagar, E.P. Gross and M. Krook, *A Model for collision processes in gases. I. Small Amplitude Processes in Charged and Neutral One-Component Systems.* Phys.Rev. **94**, 511-525 (1954)

[2] M. Krook, *Continuum equations in the dynamics of rarefied gases.* J. Fluid Mech. **6**, 523-541 (1959)

[3] C. Cercignani, *Theory and Application of the Boltzmann Equation.* Scottish Academic Press (1975)

[4] L.H. Holway, *New Statistical Models for Kinetic Theory: Methods of Construction.* Physics of Fluids **9**, 1658-1673 (1966)

[5] P. Andries, P. Le Tallec, J. Perlat, B. Perthame, *The Gaussian-BGK model of Boltzmann equation with small Prandtl numbers*, European Journal of Mechanics: B Fluids **19**(6), 813-830 (2000)

[6] F. Bouchut, B. Perthame, *A BGK model for Small Prandtl Number in the Navier-Stokes Approximation.* J. Stat. Phys. **71**, 191-207 (1993)

[7] H. Struchtrup, *The BGK model with velocity dependent collision frequency.* Continuum Mech. Thermodyn. **9**, 23-32 (1997)

[8] P. Charrier, B. Dubroca, J.-L. Feugeas, L. Mieussens, *Modèles à vitesses discrètes pour le calcul d'écoulements hors équilibre cinétique.* C.R. Acad. Sci. Paris **326**, 1347-1352 (1998)

[9] L. Mieussens, *Discrete-Velocity Models and Numerical Schemes for the Boltzmann-BGK Equation in Plane and Axisymmetric Geometries* Journal of Computational Physics **162**(2), 429-466 (2000)

[10] L. Mieussens, *Discrete velocity model and implicit scheme for the BGK equation of rarefied gas dynamics.* M3AS **10**(8), 1121-1149 (2000)

[11] I. Müller, *Thermodynamics.* Pitman, Boston 1985

[12] R.L. Liboff, *The Theory of Kinetic Equations.* Wiley and Sons, New York 1969

[13] S. Chapman, T.G. Cowling, *The mathematical Theory of Non-Uniform Gases*, Cambridge University Press (1970)

[14] G.A. Bird, Molecular Gas Dynamics and the Direct Simulation of Gas Flows, Oxford Science Publications, 1994.

[15] K. Aoki, K. Kanba and S. Takata, *Numerical Analysis of a Supersonic Rarefied Gas Flow Past a Flat Plate.* Phys. Fluids **9**(4), 1144-1161 (1997)

[16] A. Frezzotti, *Numerical Investigation of the Strong Evaporation of a Polyatomic Gas.* Proc. 17th Symp. Rarefied Gas Dynamics, 1243-1250 (1991).

[17] Y. Sone, S. Takata, *Discontinuity of the velocity distribution function in a rarefied gas around a convex body and the S layer at the bottom of the Knudsen layer.* TTSP **21**(4-6), 501-530 (1992)

[18] L. Mieussens and H. Struchtrup, *Numerical Solutions For The BGK-Model With Velocity-Dependent Collision Frequency.* Symposium on Rarefied Gasdynamics 23, AIP Conference Proceedings **663**, 320-327 (2003)